Defects Studies in β-Ga$_2$O$_3$ Using an Optimized Hybrid Functional

Ph.D. thesis

by

Quoc Duy Ho

Department 1

Physics and Electrical Engineering

University of Bremen

September-2019

Defects Studies in β-Ga$_2$O$_3$ Using an Optimized Hybrid Functional

Quoc Duy Ho

Acknowledgements

First of all, I would like to give my special thanks to my supervisor, Prof. Peter Deák, for the continuous support of my study and research, for his patience, motivation, enthusiasm, and immense knowledge. Without his encouragement and guidance, this thesis would not be finished.

My sincere thanks to Prof. Thomas Frauenheim, for giving me an opportunity to work and finish my Ph.D. thesis at Bremen Center for Computational Material Science (BCCMS), University of Bremen. His support is very important for me to accomplish my work.

I would like to thank Dr. Bálint Aradi and Dr. Christof Köhler for many technical discussions. My special thanks go to Dr. Huynh Anh Huy who introduced me to BCCMS. I also wish to express my sincere thanks to the wonderful secretaries of the BCCMS.

I would like to say thank you to the Can Tho University of Technology and to

Contents

List of Figures

List of Tables

Defects Studies in β-Ga$_2$O$_3$ Using an Optimized Hybrid Functional

Abstract

Semiconductor materials play a very important role in the development of electronic technology and they can be applied in many fields. Monoclinic gallium oxide (β-Ga$_2$O$_3$) has recently attracted a lot of attention due to its unique properties, such as wide band gap, transparency to UV and visible light, physical and chemical stability. Since good-quality β-Ga$_2$O$_3$ single crystals and thin film are already synthesized successfully, β-Ga$_2$O$_3$ can be applied in photocatalytic devices, phosphorescent and electroluminescent devices, gas sensors, and transistors. All of these applications require a full knowledge about electrically and optically active defects.

β-Ga$_2$O$_3$ is a wide band gap semiconductor, a lot of deep defect levels can be present in the gap state. For a long time, information about deep defect levels came only from photoluminescence and electron energy loss spectra. Photoluminescence (PL) measurement usually observes three emission bands, ultraviolet (UV), blue, and green, in as-grown samples and red PL is also observed upon nitrogen doping, but the lack of explanation for the origin of the PL limits the application of β-Ga$_2$O$_3$ in micro- and optoelectronic devices. Although, recently, on β-Ga$_2$O$_3$ more scientific results have been published, due to the appearance of new experimental technologies, such as deep-level transient spectroscopy and

deep-level optical spectroscopy, there is still little known about the intrinsic defects. p-type doping is another issue of β-Ga_2O_3, Mg used to be considered as a solution for p-type doping of β-Ga_2O_3 as Mg is an effective p-type dopant in GaN. Nevertheless, the experimental results indicated that Mg-doping in β-Ga_2O_3 only leads to semi-insulating.

From a theoretical point of view, the standard local density (LDA) and semi-local generalized gradient (GGA) approximation of density functional theory (DFT) played an important role in the understanding of the electrical and optical properties of defects in traditional semiconductors. Unfortunately, these fail to describe the localization of defect states and underestimate the band gap of wide band gap materials such as β-Ga_2O_3. In these cases, hybrid functionals are often applied to overcome the problems of DFT. HSE with 25% of Hatree-Fock exchange ($\alpha = 0.25$) and the screening parameter $\mu = 0.20$ are widely used for many semiconductors and give results in the best band gap. However, those parameters are not so good for ionic insulator or metal calculations, thus it is necessary to find a new optimized hybrid functional for β-Ga_2O_3. HSE, two parameters (α and μ) can be tuned to reproduce the experimental band gap and fulfill the generalized Koopman's theorem. Deák et $al.$ [2] have tuned both α and μ, and found that the hybrid functional with the parameters $\alpha = 0.26$ and $\mu = 0.00$ is the optimal HSE for β-Ga_2O_3 defects studies. This optimized hybrid functional reproduces not only the band gap, but also satisfies the generalized Koopmans' theorem.

Herein, the optimized hybrid functional and a modification of the charge correction process were utilized for β-Ga_2O_3 with the results as follows:

- A consistent description of observed carrier trapping by intrinsic defects in β-Ga_2O_3 was given. Only the gallium interstitial acts as triple shallow donors, the other intrinsic defects are deep. Both the oxygen vacancy and the interstitial are hole traps, while the gallium vacancy is the main compensating acceptor in undoped samples, in addition to small hole polarons.

- The intrinsic defects, as well as nitrogen at oxygen sites, can act as acceptors. The observed photoluminescence can be explained as recombination between a shallow electron and a hole trapped at one of the acceptors. That mechanism is suggested as a common mechanism in the wide-band gap semiconductors which can only be doped with n-type. The UV bands can be explained by the self-trapped holes states. The blue band mainly originates from singly negative Ga-O vacancies, and the green band is caused dominantly by interstitial O atoms. In N-doped samples, a nitrogen substitutional on the tetrahedral oxygen site reproduces the observed red luminescence.

- The Mg impurity introduces a deep acceptor level in β-Ga_2O_3 corresponding to a small polaron, localized at an oxygen site adjacent to the substitutional Mg. The trapped hole prefers localization at the so-called O1 site and has the superhyperfine interactions with the neighboring tetrahedrally coordinated Ga atom. The calculated hyperfine tensor agrees well with the EPR measurement. The calculated results confirm that Mg cannot act as a shallow acceptor in β-Ga_2O_3.

Chapter 1

State of the Art

1. Fields of application for Ga_2O_3

1.1.1 Subtrates for GaN devices

GaN is a very important material for optoelectronic devices, ultraviolet-blue light emitting diodes, photodetectors and lasers. [4–6] Since, GaN homoepitaxy is expensive, GaN-based devices are usually grown now by heteroepitaxy on the substrates such as silicon (Si), silicon carbide (SiC), or gallium oxide (Ga_2O_3). Ga_2O_3 substrates have many advantages compared to Si and SiC substrates. Si substrates interact with GaN in the growth environment and these substrates are not transparent to visible and ultraviolet (UV) wavelengths. SiC substrates are

1

costly and have high optical absorption in the blue region of the spectrum. In contrast, monoclinic gallium oxide (β-Ga$_2$O$_3$) substrates are transparent in visible and UV, and they can be grown by the Czochralski or the edge-defined film-fed growth (EFG) technique at relative low costs [7, 8].

1.1.2 Photocatalytic

Photocatalytic activity is a very promising research area, because it can be conducted at room temperature, low cost, and environmentally friendly. TiO$_2$ is primarily used as photocatalytic, especially in photocatalytic water spitting. When TiO$_2$ is irradiated by a UV light source, electron-hole pairs are created. The electrons and holes then can interact with water to yield oxygen and hydrogen. Compared to TiO$_2$, β-Ga$_2$O$_3$ has a much wider band gap that gives β-Ga$_2$O$_3$ a higher reductive capability. The conduction and valence band-edge of β-Ga$_2$O$_3$ is 1.1 eV higher and 2.5 eV lower than the H$^+$/H$_2$ and O$_2$/H$_2$O redox potentials, respectively [9]. In addition, Ga$_2$O$_3$ can also be used in the photoelectrolysis of CO$_2$ reduction [10] and benzene oxidation, where the oxidation capability of β-Ga$_2$O$_3$ is higher than TiO$_2$ [11]. Various Ga$_2$O$_3$ polymorphs have different photocatalytic activities. The decomposition of volatile aromatic compounds (e.g. benzene and toluene) have been tested with various polymorphs by Hou *et al.* [12] and it was concluded that β-Ga$_2$O$_3$ exhibited the best photocatalytic activities. In addition, this report also showed that the photocatalytic activity of β-Ga$_2$O$_3$ was higher compared to TiO$_2$. The main drawback associated with β-Ga$_2$O$_3$ photocatalytic activity is its wide band gap which allows β-Ga$_2$O$_3$ to absorb only the UV light.

1.1.3 Phosphorescent and electroluminescent devices

Phosphorescent and electroluminescent devices are other applications of β-$\mathrm{Ga_2O_3}$. Conventional materials used in luminescent and electroluminescent devices are primarily sulfide-based phosphors, but these materials lack primary color emissions and are chemically instable, especially in moisture conditions. In contrast, luminescent β-$\mathrm{Ga_2O_3}$-based devices are very stable physically and chemically. In addition, β-$\mathrm{Ga_2O_3}$ can also be applied in electroluminescent devices. Because of a wide band gap, β-$\mathrm{Ga_2O_3}$ can be doped with transition metals or rare-earth metals to allow for the emission of various colors. β-$\mathrm{Ga_2O_3}$ doped with manganese can radiate a visible light band around 500nm [13, 14]. When the dopant is nitrogen [15], β-$\mathrm{Ga_2O_3}$ exhibits red emissions. Those dopants are of great interest due to the fact that they are suitable to emit primary colors in full-color displays. Yellow and blue emissions can also be produced with Ce, Tm, Sn, and Dy impurities in β-$\mathrm{Ga_2O_3}$ [14]. Due to the high stability and abundant radiation of colors, β-$\mathrm{Ga_2O_3}$ attracts a lot of attention as a new material for emissive displays such as thin-film electroluminescent displays, plasma display panels, and field-emission display.

1.1.4 Gas sensors

Gas sensor devices based on $\mathrm{Ga_2O_3}$ are also attractive to many researchers, especially β-$\mathrm{Ga_2O_3}$ as an oxygen gas sensor. Oxygen gas sensor application of β-$\mathrm{Ga_2O_3}$ largely based on the correlation between conductivity and oxygen partial

pressure in annealing environments. [16] Fleicher and Meixner [17] deposited a β-Ga$_2$O$_3$ thin film layer on the top of a non-conducting BeO ceramic substrates in order to manufacture oxygen gas sensors. The oxygen gas sensors can be implemented at 1000°C and the stability of the sensors were determined for more than 150 hours. Recently, the performance of oxygen gas sensors based on β-Ga$_2$O$_3$ was studied by M. Bartic [18]. It was shown that the performance of these devices depends on the temperature with the maximum sensitivity and the shortest response time around 800°C. Besides oxygen, β-Ga$_2$O$_3$ gas sensor devices can also be used to detect CH$_4$, H$_2$, NO, and NO$_2$. [19]

All of applications need of course, a thorough knowledge of the material, especially electrically and optically of active defects. Unfortunately, there was little known about the defects in β-Ga$_2$O$_3$. Herein, I will summarize the current knowledge of β-Ga$_2$O$_3$ and discuss some open issues.

2. Current scientific knowledge of β-Ga$_2$O$_3$

There are 5 commonly identified phases of Ga$_2$O$_3$ including corundum (α), monoclinic (β), defective spinel (γ), orthorhombic (ε), and another orthorhombic phase (δ).[20–27] Among the 5 phases of Ga$_2$O$_3$, the monoclinic phase (β-Ga$_2$O$_3$) is the thermodynamically most stable.

β-Ga$_2$O$_3$ is a semiconductor with a large band gap nearly 5 eV. [28–30] Monoclinic Ga$_2$O$_3$ is usually considered to have an indirect band gap and the indirect

transition energy was found around 0.04 eV smaller than the direct transition energy. [31, 32] Later, within the framework of density functional theory and Hedin's GW approximation for single-particle excitations, Furthmüller and Bechstedt [1] reported that β-Ga$_2$O$_3$ has a direct transition at Γ point. The electron and hole effective mass of β-Ga$_2$O$_3$ can be calculated from the band structure. The electron effective mass is small and almost isotropic, 0.281 ∓ 0.005 m$_e$, [32] where m$_e$ is the free electron mass. In contrast to the electron effective mass, the effective mass of hole can be much heavier due to the flat valence band. Varley et $al.$ [32] estimated the effective mass of holes along Γ-Z direction of $\sim$40m$_e$ and $\sim$0.40m$_e$ along the Γ-A direction.

β-Ga$_2$O$_3$ samples are usually measured as a n-type semiconductor in experiment, even without intentional dopants. In contrast, p-type crystals are not produced. There are two reasons which make producing p-type β-Ga$_2$O$_3$ difficult. First of all, holes in the valence band (VB) have high effective mass. Second, the compensation by the unintentional n-type dopant in β-Ga$_2$O$_3$ [33]. By using the CVD method, Liu et $al.$ [34] doped nitrogen (N) into β-Ga$_2$O$_3$ and reported the p-type behavior of the sample. However, later in theoretical research, DFT calculations ruled out the shallow acceptor behavior of N-doped in β-Ga$_2$O$_3$, N dopant acts as a deep acceptor with an acceptor level at 1.33 eV above the valence band maximum in β-Ga$_2$O$_3$. [35]

By doping samples with Sn [36–38] or Si [39, 40] electron concentrations in the range of 10^{16}-10^{19} cm^{-3} have been reported. Unintentionally doped β-Ga$_2$O$_3$ samples were reported having carrier concentrations up to 10^{18} cm^{-3}. [41] Hall-

effect measurements were used to estimate the donor ionization energy in the range of 16-30 meV. [42] In the early years of β-Ga$_2$O$_3$ research, it was often assumed that the carriers originated from the oxygen vacancies, which act as double donors. This was explained due to the correlation between the conductivity and oxygen pressure in the annealing environment. However, the carriers originated from oxygen vacancies can only be supported at above 700°C, where the conductivity of the samples correlates with the oxygen pressure in the environment, while at low temperature, other mechanisms are used to explain. [16] An early semi-empirical quantum chemical calculation reported the vertical charge transition level of the most favorable to the oxygen vacancy is 2.8 eV below the CBM. [43] Later, hybrid functional calculations confirmed the deep donor behavior of oxygen vacancies with the transition levels $(2+/0)$ that are more than 1eV below the CBM. [32] Therefore, oxygen vacancies cannot be responsible for n-type conductivity of β-Ga$_2$O$_3$ at low temperatures. Yamaga et $al.$ [44] suggested another model that was used to explain the n-type conductivity of β-Ga$_2$O$_3$ after the observation of the EPR spectra of β-Ga$_2$O$_3$. The model explained that Si, Zr, and Hf at a gallium site will give excess electrons and those electrons are trapped by the oxygen vacancy and oxygen interstitial (V$_O$-O$_i$) pair. However, a recent study [45] has ruled out that model as the donor is very stable after annealing, where the V$_O$-O$_i$ pair is dissociated. That study assigned unintentional doped Si to the n-type conductivity in β-Ga$_2$O$_3$ at low temperature. It is now widely agreed that the origin of the n-type conductivity in β-Ga$_2$O$_3$ at low temperature is due to unintentionally doped impurities [32, 45, 46]. The hybrid functional calculations suggested that beside Si other dopants such as Ge, Sn, F and H impurities can also be doped to make n-type β-Ga$_2$O$_3$ crystals. [32]

6

For a long time, information about deep defect levels could only be derived from electron energy loss spectra (EELS) and photoluminescence (PL). A broad peak around 3.3 eV above the VBM has been measured from EELS, [47] but no interpretation was attempted. the observation of optical absorption found a series of peaks beginning at 4.48 eV. The presence of gallium vacancies (V_{Ga}) in β-Ga_2O_3 was suggested as the origin of that series [48]. Nevertheless, until now, there is no other study that justifies this assumption. Recently, with the development of technology, deep-level transient spectra (DLTS) and deep-level optical spectra (DLOS) have been used to observe n-type β-Ga_2O_3 single crystals [42, 49]. DLTS detected three levels at 0.6 eV, 0.8 eV, and 1.0 eV below the CBM in both Czochralski and edge-define film-fed grown samples. DLOS could detect deeper defects at 2.2 eV and 4.4 eV below the CBM. The traps at CBM-0.8 eV are assigned to the main compensating centers of n-type conductivity in β-Ga_2O_3. [42] However, but the data available so far did not allow identification with specific defects. In light of this, quantitatively accurate theoretical prediction of defect levels would be of high interest.

In photoluminescence (PL) measurements, three emission bands are usually observed in as grown samples, they are centered around 3.40 eV (UV), 2.95 eV (blue), and 2.48 eV (green). The UV band intensity is usually observed to be independent of impurities and diminishes fast with rising temperature, therefore, the UV luminescence bands are assigned to electrons recombination with self-trapped holes. [50] Yamaga et $al.$ [51] later found that one component of the UV PL was polarized purely in the direction of the c axis, while the other is in between the a and c direction. The existence of self-trapping of holes has been confirmed in resonant

7

photoemission studies. [52] The blue PL is usually attributed to donor-acceptor recombination [53] and the gallium vacancy (V_{Ga}) or the divacancy ($V_{Ga}+V_O$) has been suggested as the responsible acceptor, while the donors were attributed to oxygen vacancies. [53] It has been noted that the green PL in β-Ga_2O_3 was measured with specific impurities, [54] but a convincing assignment is still missing. Recent studies have shown the relative intensity of the UV, blue, and green bands correlate with the carrier concentration [55] and the stoichiometry of the samples [56]. Similarly, to the origins of the blue and green PL, a convincing explanation for these correlations has yet not been given. Besides, the three common luminescence bands in as-grown samples, red luminescence was observed in heavily nitrogen (N) contaminated nanoflakes [57] and nanowires [58, 59]. When N is doped at high concentrations, GaN clusters were observed, a band at 1.71 eV in the room-temperature PL spectrum of nanowires was assigned to substitutional N as the acceptor in a donor-acceptor recombination [58]. In nitrogen-doped spherical single crystals of $\sim$200-nm diameter, sharp peaks between 1.77 and 1.80 eV were also assigned to isolated nitrogen substitutional sites [15].

Mg is an effective acceptor dopant in GaN. [60, 61] However, recent reports [55, 62, 63] have indicated that Mg-doping in β-Ga_2O_3 leads to semi-insulating material, because Mg acceptors are too deep in the band gap. In these samples, an electron paramagnetic resonance (EPR) study by Kananen *et al.* [3] has found a hyperfine interaction of a hole with the two nearest Ga ions after X-ray irradiation and no hyperfine interaction before the irradiation. The authors proposed that a hole was trapped at a threefold-coordinated oxygen site, adjacent to a substitutional Mg on an octahedral gallium site. That model is quite reasonable because

it indicates a small hole polaron bound by the Mg ion. These polaronic states are usually found deep, which would exclude Mg as a possible shallow acceptor β-Ga_2O_3. However, until now there is no other study that can confirm this model.

The material β-Ga_2O_3 is already successfully synthesized in good-quality single crystals and thin films that make this semiconductor is a very promising candidate in applications. All of applications require a full understanding of the electrically and optically active defects. Even though the number β-Ga_2O_3 publications has recently risen, there was very little knowledge of this material and an abundance of unanswered questions. These include a satisfied interpretation of the EELS, DLTS, and DLOS peaks that are not given, the origins of the PL spectra, and the theoretical confirmation of Mg-doped behaviors which is still missing.

The objective of this thesis is to attempt to answer all of these questions and provide a clear picture of the defects in β-Ga_2O_3 by using a theoretical research method. In the next part of this thesis, the theoretical research method and explanation of usage will be discussed.

Chapter 2

Theoretical Background

1. Density functional theory

Density functional theory (DFT), the method is often used to calculate ground-state electronic structure calculations of atoms, molecules and solid state materials. The basic idea of DFT is that any properties of a many body system can be described by a functional of ground state

DFT was given a formal footing by the two theorems introduced by Pierre Claude Hohenberg and Water Kohn [64] in 1964. These relate to any system of N electrons moving under the influence of an external potential and there are two theorems.

The First Hohenberg-Kohn Theorem (HK1) states that *for any system of electrons in an external potential V_{ext} the density is uniquely determined, except for a constant, by the ground state density $\rho(r)$.*

Within the external potential, the electron density charge state $\rho(r)$ can replace the many body system. Thus, the total energy can be presented by a function of electron density $E[\rho(r)]$.

The Second Hohenberg-Kohn Theorem (HK2) states that *a universal functional $F[\rho(r)]$ for the energy of density $E[\rho(r)]$ can be defined for all electron system. The exact ground state is the global minimum for a given V_{ext}, and the density $\rho(r)$ which minimizes this functional is the exact ground state density $\rho(r)$*

$$ E = \min \left\{ F\left[\rho\left(r\right)\right] + \int \rho\left(r\right) V_{ext} dr \right\} \qquad (2.1.2) $$

The advantage of the Hohenberg–Kohn theorems is the introduction of the universal functional $F[\rho(r)]$, which is independent from the external potential. However, they do not describe the way to construct that functional.

In order to construct the universal functional, Kohn and Sham provided a theory that was later called the Kohn-Sham theory [65]

The theory states that *the ground state density of the original interacting system is equal to that of some chosen non-interacting system that is exactly soluble, with all difficult part (exchange and correlation) included in some approximate*

11

functional of the density.

Based on the Kohn-Sham theory the exact ground state density of a many body system can be described as the ground state of a non-interacting system as follows:

$$\rho_{KS}(r) = \sum_{i=1}^{N} |\psi_i(r)|^2 \tag{2.1.3}$$

The Hamiltonian of the auxiliary non-interacting system now contains the kinetic energy and the local effective potential on electrons

$$H_{KS}(r) = -\frac{1}{2}\nabla^2 + V_{KS}(r) \tag{2.1.4}$$

The ground state energy functional in the Kohn Sham approach to the full interacting many-body problem is rewritten in the form

$$E_{KS}\left[\rho\left(r\right)\right] = T_{KS}\left[\rho\left(r\right)\right] + E_H\left[\rho\left(r\right)\right] + \int \rho\left(r\right)V_{ext}(r)dr + E_{xc}\left[\rho\left(r\right)\right] \tag{2.1.5}$$

E_{xc} is the exchange-correlation that has the remain unknown terms such as the differences between kinetic energy of the interacting and non-interacting system $\Delta T[\rho(r)]$, the non-classical electrostatic energy $\Delta E_{ee}[\rho(r)]$.

After applying the variational principle for the equation (2.1.5) and the Lagrange multiplier method with the orthogonalization constraint, we get the Kohn-

Sham equation for the single-particles as:

$$[-\frac{1}{2}\nabla^2 + V_{KS}(r)]\psi_i(r) = \varepsilon_i\psi_i(r) \qquad (2.1.6)$$

where

$$V_{KS}(r) = V_{ext}(r) + \frac{\delta E_H\left[\rho\left(r\right)\right]}{\delta\rho\left(r\right)} + \frac{\delta E_{xc}\left[\rho\left(r\right)\right]}{\delta\rho\left(r\right)} = V_{ext}(r) + V_H(r) + V_{xc}(r) \quad (2.1.7)$$

Equations (2.1.3), (2.1.6), and (2.1.7) are usually called the Kohn-Sham equations. The Kohn-Sham equations are solved by a self-consistent method. First, trial wave-functions are used to form an initial density. Then the V_{KS} is calculated from the initial density, the Schrödinger equations are solved to provide wave-functions, and a new density is calculated. The procedure is repeated until the input and output densities are identical. The approach of Kohn-Sham theory simplifies the Schrödinger equation and allows this to be calculated. However, the exchange-correlation is extremely complicated and unknown. Thus, the approximation for that part is needed.

2. Local density approximation and the generalized gradient approximation

Local density approximation (LDA) is an exchange-correlation approximation based on the idea that the electron density can be locally treated that of an uniform gas. Therefore, each point of the system has the same exchange correlation

energy as a uniform electron gas of the same density. This approximation is true in a system where the density slowly varies. The LDA exchange correlation can now be written as:

$$E_{xc}^{LDA}[\rho(r)] = \int \rho(r)\, \varepsilon_{xc}[\rho(r)]\, dr \qquad (2.2.8)$$

Where $\rho(r)$ is the electron density, $\varepsilon_{xc}[\rho(r)]$ is the exchange-correlation density. The exchange-correlation density is given [66]

$$V_{KS}^{LDA}(r) = \frac{\delta E_{xc}[\rho(r)]}{\delta \rho(r)} = \varepsilon_{xc}[\rho(r)] + \rho(r)\frac{\partial \varepsilon[\rho(r)]}{\partial \rho(r)} \qquad (2.2.9)$$

LDA assumes that energy of the real electron density is the same at every point in space. Thus, it fails to explain a system where the density changes with respect to position rapidly.

For the rapidly changing density, generalized gradient approximation (GGA) exchange-correlation should be used. GGA can be considered as an improvement of LDA, whereas the GGA depends on both of the density at a point (as in the LDA) and the gradient of the density. The exchange term of the GGA can be expressed as follow:

$$E_{xc}^{GGA}[\rho(r)] = \int \rho(r)\, \varepsilon_{xc}[\rho(r), \Delta\rho(r)]\, dr \qquad (2.2.10)$$

By adding terms of the density gradient, GGA can overcome the problems of LDA in the calculation of the non-homogeneity of the true electron density.

3. Failure of DFT with local and semi-local approximation

Although, LDA and GGA of density functional theory played an important role in understanding the electrical and optical properties of defects in traditional semiconductors, they are not adequate for defects in wide band gap semiconductors. [67, 68].

One of the issues of LDA/GGA is the deviation from the correct piecewise linear behavior of the total energy as a function of the occupation numbers. The (semi) local exchange functionals do not show a derivative discontinuity at integer occupation number at all, so that will be small in the total energy as well (some discontinuity coming from the kinetic energy). This is the reason of the underestimated gap in LDA/GGA calculations. For example, both of LDA and GGA predict the quasi particle band gap of anatase TiO_2 much smaller the experimental optical band gap, 1.98 eV and 2.12 eV [69] compare to 3.2 eV [70]. It also often happens that actual gap levels are hidden in the bands, being incorrectly unoccupied (donors) or occupied (acceptors).

Another issue of LDA/GGA is the convex nature of the total energy, as a

function of the fractional occupation numbers, leads to artificial delocalization of defect states. Since the localization of a defect state usually determines the position of the corresponding level in the gap directly, the artificial delocalization makes the prediction of gap states inaccurately. In addition, in wide band gap material, small polaron states often occur, but LDA/GGA calculations are usually missed.

4. Hybrid functionals

Since LDA and GGA of density functional theory usually cannot handle wide band gap oxides, it is necessary to develop a new approximation that can overcome the issues of LDA/GGA. It is shown that GGA exchange gives a convex behavior (red curve in Fig. 2.1) of total energy as a function of occupation number while Hartree-Fock (HF) gives a concave behavior (blue curve in Fig. 2.1). Thus, the combination of them may give a linear behavior of total energy (dash green line in Fig. 2.1). The density functional theory calculations with the exchange that is the combination between the exchange functional of LDA/GGA and the Hartree-Fock non-local type exchange is usually called hybrid functional calculations.

In recent years, HSE hybrid functionals have emerged as a powerful tool for semiconductors calculations, especially screened hybrids [71, 72], and particularly the HSE06 functional of Heyd, Scuseria, and Ernerhof. [73, 74] Specifically, HSE-type hybrids are semi-empirical functionals where the exchange functional is mixed with the ratio α of the Hartree-Fock exchange and (1-α) of the GGA. In a
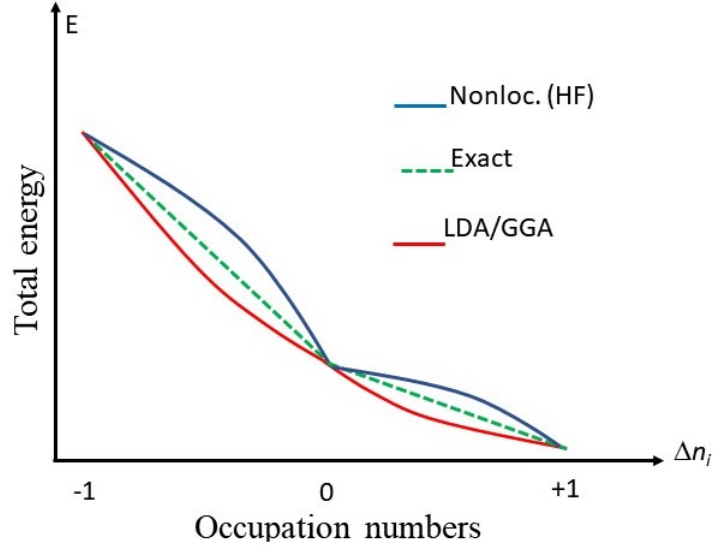
Figure 2.1: The total energy as a function of occupation numbers

real system, the interactions between electrons are screened and the contribution of the long-range exchange is small or disappears. To account for the screening, the mixing is phased out by an error function beyond a distance $2/\mu$, where μ is the screening parameter. The exchange of the HSE is given as follows:

$$E_{xc}^{HSE} = aE_X^{HF,SR}(\mu) + (1-a)E_X^{PBE,SR}(\mu) + E_X^{PBE,LR}(\mu) \qquad (2.4.11)$$

Where μ is the screening parameter which defines the range of the HF correction with the following error function:

$$\frac{1}{r} = \frac{\text{erfc}(\mu r)}{r} + \frac{\text{erf}(\mu r)}{r} \qquad (2.4.12)$$

In accordance with the argumentation of Ref[75] for single bonds, and similar to

17

the unscreened PBE0 hybrid [76], the optimal ratio of the HF exchange was found to be $\alpha = 0.25$ also in HSE06. The screening parameter is usually set to $\mu = 0.20$. The HSE06(0.25,0.20) results in the best band gap for many semiconductors. Although, the value chosen in HSE06 works well with a medium-size gap (and medium screening), with a few exceptions, it does not work well in ionic insulators (week screening) and metals (strong screening) [77, 78]. Obviously, the screening parameter plays a very important role in the success of HSE-type functionals [72, 79]. However, when the standard HSE06 underestimates the band gap, only α is often tuned, and the role of the screening parameter is forgotten. In doing so, the issue of the localization of defect states is not usually considered, even though it has been shown that accurate description of small polaron states can only be expected if the generalize Koopmans' theorem is satisfied [80], i.e. if the total energy is a linear function of the fractional occupation number. It is known that an increasing ratio of the HF exchange percentage will not only increase the band gap, but also makes the total energy more concave leading to a stronger localization. Therefore, HSE-type hybrids offer an opportunity for mimicking the self-interaction-free functional of exact DFT by error compensation. Tuning both of α and μ can reproduce the experimental ban gap and a piece linear function of the occupation numbers.

Deák, *et al.* [2] has tuned both α and μ to find out an optimized hybrid functional for $\beta\text{-Ga}_2\text{O}_3$ calculations. This resulted in $\alpha = 0.26$ and $\mu = 0.00$ as the optimized parameters for $\beta\text{-Ga}_2\text{O}_3$ calculations. The research found that the new optimized hybrid functional HSE(0.26,0.00) not only reproduces the experimental band gap, but also fulfills the Koopmans' theorem. That fulfilment suggests that the new optimized hybrid can give the accurate localization of defect states in

β-$\mathrm{Ga_2O_3}$. The work herein uses HSE(0.26,0.00) to study electrical and optical properties of intrinsic defects, photoluminescence, and the hyperfine interaction in β-$\mathrm{Ga_2O_3}$.

Chapter 3

Calculation Details

1. Electronic structure calculations

The calculations herein were conducted with use of the Vienna Ab-initio Simulation Package (VASP 5.3.3) and the projector augmented wave method (PAW) [81–83]. The semi-core d electrons of gallium were treated as part of the valence shell. The plane-wave basis set was truncated at 420 eV and the kinetic energy cut-off for the augmentation charges was 840 eV. The equilibrium geometry was determined for the primitive unit cell with a $4 \times 4 \times 4$ Monkhorst-Pack (MP) k-point set [84], based on constant volume relaxations and fitting to the Murnaghan's equation of state [85]. The band structure of β-Ga_2O_3 was calculated with a 10 atoms unit cell, which is a base center monoclinic cell. To ensure an unbiased

description of relaxation in all directions, defect calculations were done in an 160-atom supercell with the dimensions of 12.25Å $\times$ 11.58Å $\times$ 12.16Å (1 $\times$ 4 $\times$ 2 of the base-center monoclinic cell in the a, b, and c directions). That is the maximum our computer can afford, the next symmetric multiple would contain 1280 atoms. The convergence condition of 10^{-4} eV was applied for the self-consistent electronic energy and the relaxation of all ions were carried out until the force on each ion was smaller than 0.02 eV/Å. Defect calculations were carried out with the Γ-approximation for the Brillouin zone sampling. Convergence of the k-point sampling was confirmed with the gallium vacancy by applying a non-Γ-centered 2 $\times$ 2 $\times$ 2 MP-set. The difference of the charge transition level (2-/3-) between the 2 $\times$ 2 $\times$ 2 MP-set and the Γ-approximation calculation was found to be 0.02 eV.

2.   Charge correction

The need for charge correction in supercells arises from the spurious Coulomb-interaction of repeated charges, and requires the dielectric constant of the material, for which the established experimental data have been used. In the following we will need the ionized state of the defect with the geometry fixed at that of the neutral one (vertical ionization), or at the equilibrium geometry of the charged state (adiabatic ionization). In the first case, obviously, the high frequency dielectric constant ε_∞ must be used. In the second case, the static dielectric constant ε_0 would be relevant in principle, because of the ionic screening. However, in the cases where $\varepsilon_0 \gg \varepsilon_\infty$, much too shallow adiabatic charge transition levels are obtained this way, while using ε_∞ reproduces the experimental value better [86].

The explanation probably is that relatively large supercells describe a substantial part of the ionic screening explicitly, and using the bulk value of ε_0 amounts to double-screening. β-Ga_2O_3 has a value of ε_0 which is around 3 times larger than ε_∞. Thus, the calculated average high-frequency (bulk) dielectric constant (3.55), found by Furthmüller et. al [1] i.e., 3.55, was used for both of adiabatic and vertical ionization. For charged defects in the supercell, the charge correction method of Freysoldt, Neugebauer, and Van de Walle [87]. was applied to correct for the artificial interactions between repeated images. The localized defect levels were corrected using the relation $\varepsilon_{\text{corr}}^{\text{level}} = -2E_{\text{corr}}^{\text{tot}}/q$, as derived by Chen and Pasquarello [88].

3. Photoluminescence calculations

I have investigated a common mechanism to explain all observed PL bands, namely electron recombination with a trapped hole, as shown in Fig. 3.1. From the view point of my calculation in a limited-size supercell (resulting, at best, in a 100-meV accuracy of the PL energy) there is no difference between an electron in a shallow donor state and a conduction band electron bound by the trapped hole. Therefore, for the sake of computational simplicity, only bound excitons were considered, with the holes trapped at various defects. The equilibrium geometry of the bound exciton was relaxed under constraint of the orbital occupations, i.e., the electron-hole interaction was explicitly taken into account. The spin multiplicity was kept constant during the whole process shown in Fig. 3.1
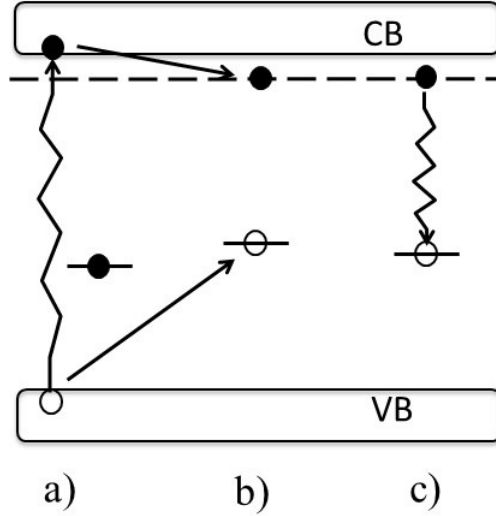
Figure 3.1: PL mechanism in β-Ga_2O_3: (a) excitation, (b) formation of a bound exciton (or a shallow donor-trapped hole pair), (c) emission

Having relax the geometry of the bound exciton in the Γ-point approximation, the total energy at the final geometry was recalculated with a (non-Γ-centered) $2 \times 2 \times 2$ Monkhorst-Pack set [84], applying band-filling correction [89]. These calculations are extremely demanding, so larger k-point sets were not possible. Note that hybrid functional calculations with small k-point sets are problematic if the screening parameter is zero, so I applied the correction described in footnote 86 of Ref [2]. The energy of the final state after recombination was calculated at fixed geometry with releasing the occupation constraint, using the same $2 \times 2 \times 2$ k-point set. The PL energy is the difference between the two total energy. In PL calculations, charge corrections (with ε_∞) were also applied for defects charge state, but note that the excited and final state have the same charge state. Therefore, the contribution of charge correction is small in PL calculations.

23

4. Hyperfine parameters

The hyperfine tensor that describes the interaction between a nuclear spin and the electronic spin distribution consists of the isotropic Fermi-contact and anisotropic dipolar term. The Fermi-contact requires calculating the spin density at the nuclear sites that carry a nuclear spin. This interaction occurs when the electron is inside the nucleus, electron in the s orbital exhibit this kind of interaction. The dipolar interactions depend on the distance between the electron and the nuclei as well as the orbital shape. After a paramagnetic defect state had been relaxed, the hyperfine tensor was calculated with the electron spin density from the previous calculation. The nuclear gyromagnetic ratios of -3.3416, 10.2477, and -5.772 were used for Mg, Ga, and O, respectively.

Chapter 4

Results and Discussion

1. On the bulk of β-$\mathbf{Ga_2O_3}$

The geometry of the primitive cell is optimized and the band structure is calculated by using the (nearly) ideal HSE(0.26,0.00). The band structure is shown in comparison with the GW results of Ref. [1] in Fig. 4.1. As can be seen, the overall agreement is excellent, even though the only experimental datum used in the fitting of the HSE parameters was the minimum band gap, which is naturally well reproduced by the GW calculation, too. (Note that the k-points between the high symmetry points of the Brillouin-zone were chosen differently in the two calculations and that gives rise to small deviations in the interpolation by spline-fitting.)
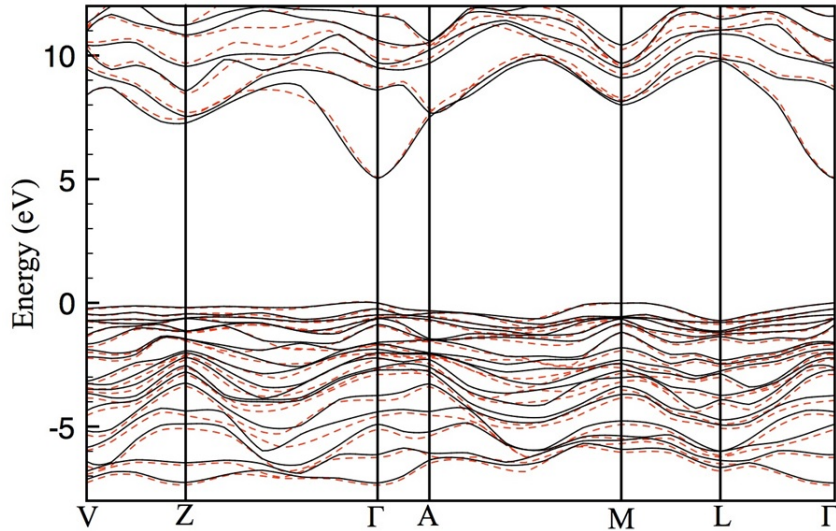
Figure 4.1: The band structure of β-Ga$_2$O$_3$, calculated by the HSE(0.26,0.00) hybrid (black solid lines) and by HSE(0.25,0.20)+G$_0$W$_0$ in Ref. [1] (red dashed lines). The band gaps are direct at Γ: 5.02 eV and 5.04 eV, respectively.

The HSE(0.26,0.00) calculation results in a direct band gap 5.02 eV, in good agreement with the value of 5.04 eV in Ref [1] both at the respective optimized geometry. Optical experiments also support the direct nature of the gap [29]. The lattice parameters are compared in Table 4.1. Based on the good results achieved for the perfect system, I apply the optimized hybrid now to calculate intrinsic traps in β-Ga$_2$O$_3$.

2. Electronic properties of defects

Fig. 4.2 shows the 160-atom perfect β-Ga$_2$O$_3$ supercell used for defect calculations. The y direction is parallel to the c and the z direction to the b axis.

Table 4.1: Comparison of the calculated and experimental lattice parameters of β-Ga_2O_3.

	GGA-AM5 [1]	HSE(0.35,0.20) [90, 91]	HSE(0.26,0.00) this work	Expt. [30]	Expt. [92]
$a[\text{Å}]$	12.29	12.27	12.25	12.23	12.21
$b[\text{Å}]$	3.05	3.05	3.04	3.04	3.04
$c[\text{Å}]$	5.81	5.82	5.79	5.81	5.80
$\beta[^\text{o}]$	103.8	103.8	103.8	103.8	103.8

There are three non-equivalent oxygen sites. O1 and O2 are trigonally coordinated, with the plane of the neighboring Ga-atoms approximately parallel to the c-axis for the former and orthogonal for the latter. O3 is tetrahedrally coordinated. The Ga-atoms are either in a tetrahedral (Ga1) or in an octahedral (Ga2) coordination.

Besides the vacancies at all nonequivalent oxygen (V_O) and gallium (V_O) sites, I also investigated oxygen (O_i) and gallium (Ga_i) self-interstitials. Gallium atoms can occupy interstitial sites with tetrahedral or octahedral coordination, the latter being about 2 eV lower in energy. This structure relaxes eventually into an interstitialcy configuration (Fig. 4.3a) by pushing two nearest-neighbor lattice gallium atoms into tetrahedral interstitial sites, with a further energy gain of 0.72 eV. This is the lowest energy configuration for Ga_i have been found. The lowest energy oxygen interstitial in HSE(0.26, 0.00) calculation also differs from the one investigated in Ref [93]: The split-interstitial configuration (Fig 4.3.b) is found to have the lowest energy.

27
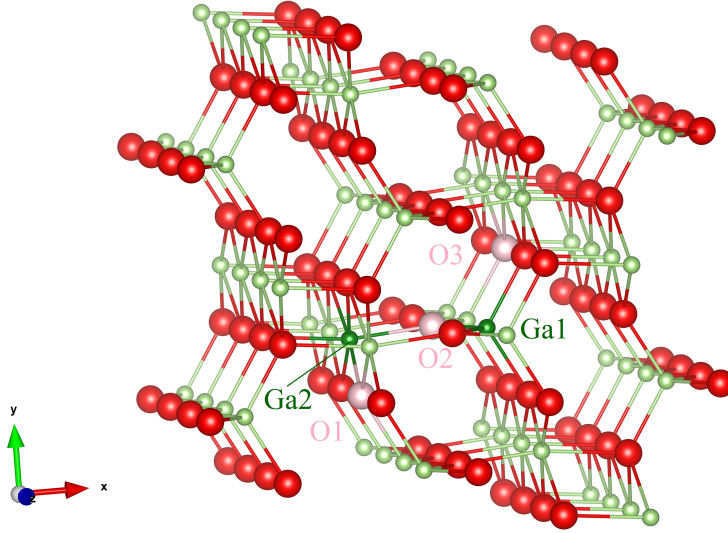
Figure 4.2: The 160-atom supercell (Ga light green and O red spheres), showing the different non-equivalent positions for oxygen (pink) and gallium (dark green).

The formation energies of defects in different charge states can be calculated as follows:

$$E^f\left[X^q\right] = E_{tot}\left[X^q\right] - E_{tot}\left[bulk\right] - \sum_i n_i \mu_i + qE_F + E_{corr}^q \qquad (4.2.13)$$

Where:

- $E_{tot}\left[X^q\right]$ is total energy of the defect X in charge state q.

- $E_{tot}\left[bulk\right]$ is total energy of the perfect supercell.

- n_i indicates the number of atoms that have been added ($n_i > 0$) to or removed ($n_i < 0$) from the supercell to form the defect.

- μ_i is the chemical potential of the atom in the reservoir corresponding to the growth conditions.

- E_F is the Fermi-level position between the VBM and CBM.

- E_{corr}^q is the charge correction energy.

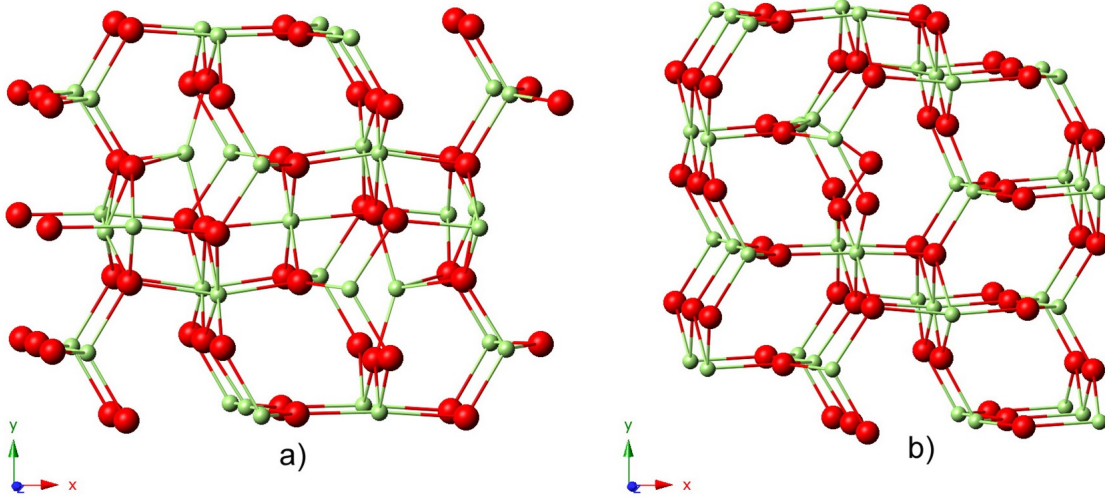**Figure 4.3:** The Ga-interstitialcy Ga_i (a) and the O split-interstitial O_i (b).

The formation energies of the intrinsic defects in different charge states are shown in Fig. 4.4, as a function of the Fermi-level position between the calculated VBM and CBM (i.e., at 0K). Fig. 4.4a corresponds to the most extreme oxygen-rich condition, where the chemical potential of oxygen is the energy of an oxygen atom in the O_2 molecule (at 0 K), $\mu_O = \frac{1}{2}\mu^{O_2}$. Fig. 4.4c shows the extreme gallium-rich case, where $\mu_{Ga} = \mu^{Ga_{metal}}$. These two cases are the theoretical limits of the chemical potentials but are never being even remotely realized experimentally. Therefore, I think it is informative to show the stoichiometric condition (Fig. 4.4b), where the defect-related gallium and oxygen deficiencies (or excesses) match the stoichiometric ratio of 2:3. I believe that high-temperature single-crystal growth methods in ambient atmosphere are between this stoichiometric and the extreme

oxygen-rich case (closer to the former). The high-energy limit is an extrapolation of the equilibrium Fermi-level position to the temperature of growth, based on observed carrier concentrations in the order of 10^{17} cm^{-3} in unintentionally doped n-type samples [42]. The low-energy limit is the estimated position of the quasi-Fermi-level for holes, due to the heat radiation of the sample [94, 95]. The quasi-Fermi-level for the majority carriers (electrons) is practically identical with the equilibrium Fermi-level [94].
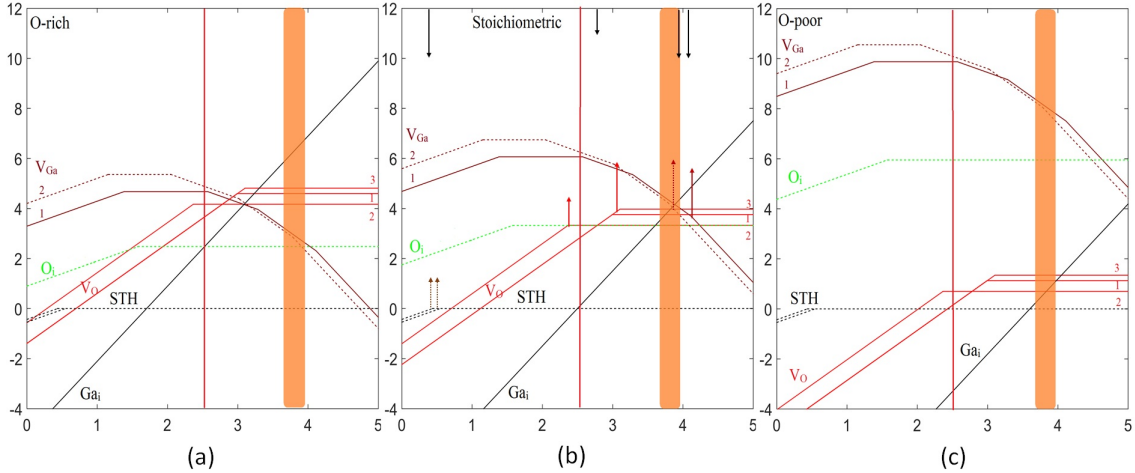
Figure 4.4: Defect formation energies (eV) as a function of the Fermi-level position between the VBM and the CBM for extreme oxygen-rich (a), stoichiometric conditions (b), and extreme oxygen-poor (c) growth conditions. The Ga$_i$ is indicated by black, V$_O$ by red, V$_{Ga}$ with dark red, O$_i$ by green dotted, and the self-trapped hole (STH) with the black dotted lines.

At high growth temperatures and moderate n-type doping, the formation energy of O$_i$ is smaller than that of V$_{Ga}$. The former is a donor, electrically inactive in the corresponding Fermi-level range, while the latter is an acceptor. With decreasing temperature and increasing concentration of donor impurities, the Fermi-level

moves higher in energy, and the acceptor-type V_{Ga} becomes energitically preferred. Therefore, V_{Ga} must be the major compensating defect for n-type doping (as suggested also in Ref [96]). While O_i would act as a hole trap if the Fermi-level moved close to the VBM. In contrast, Ga_i is a shallow triple donor. At the Fermi-level range indicated in Fig. 4.4, it can compete with V_O under oxygen-poor conditions and contribute to the observed intrinsic n-type conductivity. This assumption is supported by the observation that annealing in oxygen removes shallow donor defects [42]. If extrinsic n-type doping or decreasing temperature moves the Fermi-level closer to the CBM, V_O becomes dominant. Its level is, however, too deep to act as donor.

My calculated formation energies for the neutral defects are similar to the theoretical research of Varley *et al.* [96, 97] and Zacherle *et al.* [93]. The adiabatic charge transition levels are, however, quite different (Table 4.2). The difference stems from both the change in the HSE parameters and from the use of ε_∞ instead of ε_0 in the charge correction. More details can be found in Ref [2].

I would also like to note that the defects investigated here are not "atomically localized", so their charge transition levels shift with respect to the average electrostatic potential, as the parameters are tuned [98]. The shift depends on the localization (distribution of the square of the one-electron wave function) and is different for the various defects. Therefore, the relative position of the charge transition levels also changes when comparing $V_{O1,2}$, and V_{O3} or V_{Ga1} and V_{Ga2}, because the removed atoms have different coordination in these cases (threefold vs. fourfold in case of oxygen and fourfold vs sixfold in case of gallium), which leads

to quite differently distributed wave functions.

Table 4.2 also compares the calculated data (for HSE(0.26,0.20) the upward-pointing arrows in Fig.4.4b) with levels observed by DLTS and DLOS in single crystals grown at high temperature (downward-pointing arrows in Fig.4.4b). Ingebrigtsen *et al.* [99] have suggested that the so-called E2* center, with a level at CBM – 0.75 eV, is the main compensating acceptor in the unintentionally doped *n*-type samples. Varley *et al.* [96] have proposed that gallium vacancies, which have a low formation energy in oxygen-rich samples, can act as such compensating acceptors; however, their calculated charge transition level for V_{Ga1} is almost 1 eV deeper than the E2* level. With the optimized hybrid and using ε_∞ for correction, that level is now at CBM – 0.67 eV, i.e., within 0.2 eV of both DLTS results. Although further experiments are needed to confirm the assignment, this near coincidence is a strong indication that our procedure is correct. Another peak from the DLTS is E3 located ∼1eV below the CBM, this peak was found with varying concentration in different experimental samples [42]. I assign that peak to the charge transition level (2-/3-) of V_{Ga2} with a transition level at CBM - 1.16.

A further justification of our procedure comes from the interpretation of the DLOS center at CBM – 4.40 eV [49]. DLOS allows to deduce also the Franck-Condon factor, i.e., the energy difference between the adiabatic and the vertical charge transition level. For this center it was found to be 0.45 eV, whereas the band gap was measured to be 4.84 eV [49]. The fact that the vertical transition (4.40 + 0.45 eV) nearly coincides with energy of a VBM – CBM excitation, and the indication for minority carrier hole photoemission to the valence band [49], make

Table 4.2: HSE(α, μ) adiabatic charge transition levels with respect to the calculated CBM (eV), in comparison with experimental values obtained at room temperature.

Level	corrected with ε_0			corrected with ε_∞	Expt.	Expt.
	HSE (0.35,0.20) [32, 96]	HSE (0.30,0.20) [93]	HSE (0.26,0.00) present	HSE (0.26,0.00) present		[49]
V_{Ga1}(-2/-3)	-1.62	-2.27	-1.64	0.67	-0.75(DLTS) E2* [a]	
V_{Ga2}(-2/-3)	-1.83	-1.93	-2.12	-1.16	-1.04(DLTS) E3 [b]	-1.00 (DLTS)
V_{O1}(+2/0)	-1.52	-1.82	-1.71	-2.10		
V_{O2}(+2/0)	-2.13	-2.42	-2.29	-2.68		-2.16 (DLOS)
V_{O3}(+2/0)	-1.26	-1.52	-1.56	-1.95		
h^+1(+/0)			-4.41	-4.61		-4.40 (DLOS)
h^+2(+/0)			-4.31	-4.50		

[a] [99]

[b] [42]

it likely that this level corresponds to a self-trapped hole in a small polaron state (h_{ST}^+), which is known to occur in β-Ga$_2$O$_3$ [51–54, 56]. Fig. 4.5 shows calculated small hole-polarons trapped near O1 and O2 sites. (no self-trapping at O3 has been found.) The calculated adiabatic charge transition levels are shown also in Table 4.2, and they are in good agreement with the DLOS level. (In this case the optimization of the HSE parameters and the change in the charge correction procedure contributes about equally to the agreement.)
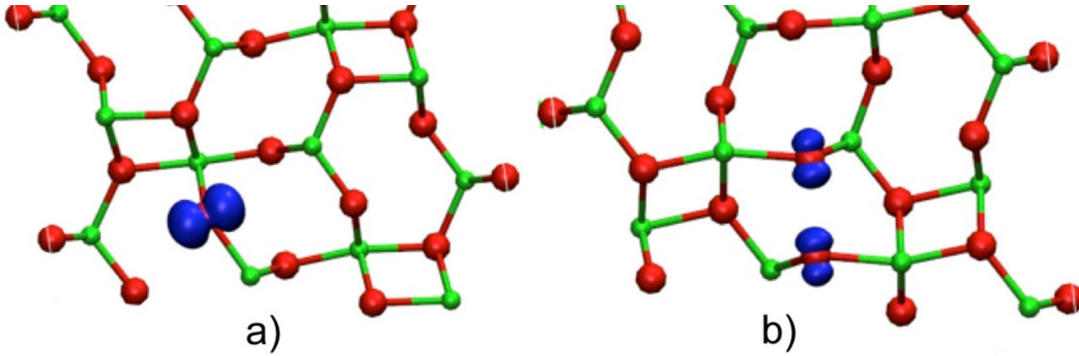
Figure 4.5: The ball-and-stick structure of β-Ga$_2$O$_3$, blue lobes representing a hole trapped in a small polaron state (h_{ST}^+) near an O1 (a) and between two O2 (b) sites. No hole self-trapping was found at O3.

The upward arrows (calculated adiabatic charge transition levels) and the downward arrows (DLTS/DLOS levels) in Fig. 4.4 show a reasonably good match, so it is tempting to interpret the low concentration DLOS center with level at CBM – 2.16 eV in the somewhat oxygen rich single crystals as the center of weight of the calculated (2+/0) levels of the oxygen vacancies (CBM – 2.24 eV), since the formation energy of V_O is still relatively low under moderately oxygen-rich growth conditions. (As shown below, the corresponding vertical transitions of the oxygen vacancies also fits the EELS peak observed in oxygen-poor samples.)

The remaining experimental data on intrinsic defects of β-Ga_2O_3 are the broad EELS peak at 3.3 eV [47] and a series of optical absorption peaks beginning at 4.48 eV [48]. Both can be interpreted as vertical electron transitions from the defect to the CBM. The EELS experiment was carried out on films obtained by oxidizing a CoGa alloy at 800K in vacuum, with an oxygen partial pressure of 10^{-6} mbar, i.e., under oxygen-poor conditions. The optical absorption spectrum was taken on small crystals grown by the Verneuil-method, which are likely to be oxygen-rich.

Table 4.3: Vertical donor ionization energies (eV).

Defect state	Defect-to-CBM	Experiment
O_i^0	4.33	
V_{Ga1}^0	4.58	4.48, 4.61, 4.73, 4.85, 4.91 [a]
V_{Ga2}^0	4.75	
V_{O1}^0	3.34	
V_{O2}^0	3.95	3.33 [b]
V_{O3}^0	3.15	

[a] [48]

[b] [47]

Due to the fulfillment of the generalized Koopmans' theorem of the HSE(0.26,0.00), defect-to-band transition energies can be obtained from the relative position of the Kohn-Sham level with respect to the band edge, as shown in Table 4.3.

In Ref [48], it was argued that the observed optical absorption is related to the

excitation of electrons from V_{Ga2} defects in an ordered array to the CBM. Under oxygen-rich conditions the gallium vacancies are, indeed, the dominant defects in n-type crystals and, as shown in Fig. 4.4, they have a $(+/0)$ donor transition level, i.e., they can be ionized also positively. The corresponding vertical transition energies of V_{Ga1} and V_{Ga2} are very well in the range of the observed optical absorption. However, as can be seen in Table 4.3, the other important intrinsic defect under O-rich conditions, O_i, can also give rise to an optical absorption band in this range.

In oxygen-poor samples the dominant intrinsic defects are Ga_i and V_O. The former is very shallow but the latter produces an optical absorption band which can very well account for the observed feature in EELS (see Table 4.3).

3. Photoluminescence

In this section, I investigated the possibility of explaining all of the aforementioned PL bands with a common mechanism, namely recombination of a weakly localized electron with a trapped hole. Table 4.4 shows the calculated PL energies. The values obtained for N_O at the most stable sites are in very good agreement with the observed peaks in N-doped single crystals, [15] showing that our numerical values are reliable.

The UV band observed in the PL spectrum of β-Ga_2O_3 seems to be independent of the prehistory of the sample and particularly of impurities, so it is mostly

Table 4.4: PL energies calculated for the hole trapped at various intrinsic defects or a substitutional N_O, in comparison to experiment (in eV).

Defect	Site	HSE(0.26,0.00)	Color	Experiment
STH	O1	3.7	UV	3.6 [55]
	between two O2-s	3.5	UV	3.2-3.4 [55]
$(V_{Ga} + V_O)^{1-}$	Ga1-O1	2.9	**Blue**	3.0 [55]
V_{Ga}^{1-}	Ga2 (octahedral)	3.0	Blue	
V_{Ga}^{2-}	Ga1 (tetrahedral)	2.7	Blue	2.8 [55]
O_i^0	split with O1	2.3	**Green**	2.4 [55]
V_{Ga}^{2-}	Ga2 (octahedral)	2.3	Green	
V_{Ga}^{1-}	Ga1 (tetrahedral)	2.3	Green	
V_O^0	O1 (trigonal)	1.6	IR	
V_O^0	O2 (trigonal)	2.0	IR	1.8 [58]
V_O^0	O3 (tetrahedral)	1.7	IR	
V_{Ga}^{3-}	Ga2 (octahedral)	2.0	Red	
V_{Ga}^{3-}	Ga1 (tetrahedral)	1.4	IR	
N_O^0	O1 (trigonal)	1.8	**Red**	1.7-1.8 [15, 58]
N_O^0	O2 (trigonal)	1.8	**Red**	
N_O^{1-}	O3 (trigonal)	2.3	Green	

assumed to be due to emission upon the recombination of the self-trapped exciton, $h_{ST}^+ + e_{CBM}^-$. The band is usually decomposed into two components around 3.6 eV and 3.2 eV [51, 55, 56]. While the second one is polarized purely in the direction of the c axis, the first one has both c and a components [51].

I calculate for exciton recombination are 3.7 eV and 3.5 eV, when the hole is trapped at the O1 or between two O2 sites, respectively. These values are fairly close to the observed ones and, in addition, the direction of the O_{2p}-like hole state (pointing in the $a+c$ and in the c direction, respectively, see Fig. 4.5) is in line with the polarization properties.

The oxygen vacancy in β-Ga$_2$O$_3$ is not a shallow donor. [32, 43, 55] According to Fig. 4.6, its donor level is deeper than 2 eV from the conduction band (CB). Since acceptor levels in β-Ga$_2$O$_3$ tend to be deep to hyperdeep [100], V$_O$, as a donor, cannot possibly give rise to PL in the visible (the shallow donor states in β-Ga$_2$O$_3$ are provided by unintentional doping [32] or by Ga$_i$ [55].) In principle, V$_O$ could participate in the PL as a hole trap, however, our results show that this can only give rise to emission between 1.6 and 2.0 eV. This is in line with the observed red emission in nominally nitrogen-free nanowires [58] but excludes oxygen vacancies as the origin of the blue and green PL bands.

Based on Table 4.4, and considering the relative stabilities of the defects (Fig. 4.6), the blue PL is assigned to the divacancy (V$_{Ga}$ + V$_O$), and the green one to the oxygen interstitial O$_i$. These assignments can be justified the following way. Onuma *et al.* [55] have studied the effect of free electron concentration on the intensity
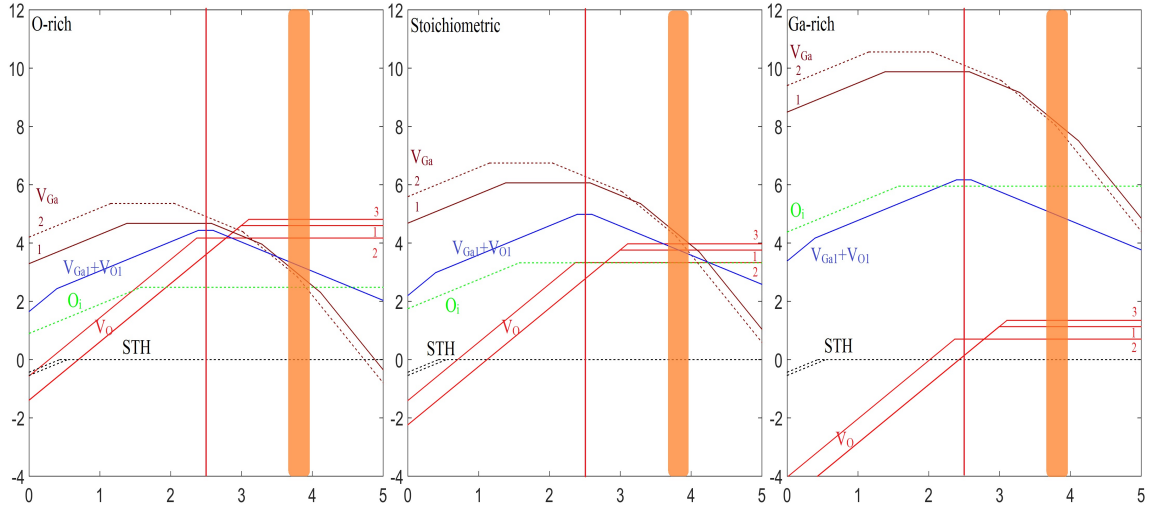
Figure 4.6: Formation energies (eV), as a function of the Fermi-level position. The shaded vertical column indicates the estimated Fermi-energy range in undoped (i.e., unintentionally n-type) samples. [2] The range to the right corresponds to intentionally n-doped, while the area to the left (down to midgap, as indicated by the vertical line) to compensated samples. The diagrams on the left and right correspond to extreme O- and Ga-rich conditions, respectively, while the one in the middle describes the stoichiometric case.

of the PL, in samples grown by the floating zone method. (It should be noted, that they have decomposed the UV band into three components.) With respect to the nominally undoped samples (carrier concentration $\sim 8.10^{16} \text{cm}^3$), the intensity of the blue band has strongly decreased in the intentionally Si-doped ($\sim 5.10^{18} \text{cm}^3$) sample, while the green luminescence was only substantial in the semi-insulating sample, compensated by Mg-doping. This behavior can be explained if one considers the stoichiometric part of Fig. 4.6. In the Fermi-energy range corresponding to as-grown samples, V_{Ga} is stable in the (2-), $(V_{Ga} + V_O)$ in the (1-) charge state. The formation energy of the divacancy is lower than those of the isolated V_{Ga} defects, so hole trapping should dominantly occur at $(V_{Ga} + V_O)^{1-}$, leading to a blue emission energy of 2.9 eV. The V_{Ga}^{2-} defects (in lower concentration) can contribute a shoulder in the blue at 2.7 eV (tetrahedral site) and some green at 2.3 eV (octahedral site). Contribution to green PL also comes from neutral O_i. In intentionally n-doped samples, the Fermi-level moves up, and the stable charge state of the V_{Ga} defects becomes (3-), with a formation energy much lower than that of $(V_{Ga} + V_O)^{1-}$ and O_i in this range. Therefore V_{Ga}^{3-} is expected to become the majority hole trap. However, V_{Ga}^{3-} can only give rise to emission in the IR-red range. This explains the intensity decrease of the blue and green PL (with $(V_{Ga} + V_O)^{1-}$ still contributing a small amount). In contrast, if the Fermi-level moves down due to compensation doping, O_i^0 is becoming the majority hole trap, explaining the increase of the green PL. It should be noted that in-growth doping on the cation site can only be achieved by shifting the conditions towards O-rich growth. Comparing the left and the middle diagram in Fig. 4.6, this means a considerable lowering in the formation energy of V_{Ga}^{1-}. This should also lead to some increase of the blue PL at 3.0 eV due to V_{Ga}^{1-} at the octahedral site, as indeed observed [55]. Víllora *et al.* [56] have studied the effect of oxygen treatment

on the PL of β-Ga$_2$O$_3$. They have found that prolonged annealing at 900 ^{o}C in O$_2$ has led to a semi-insulating sample, and the PL was dominated by the green band. Obviously, such a treatment leads to oxygen-rich (gallium poor) conditions, diminishing the concentration of the gallium interstitials (Ga$_i$) which are intrinsic shallow donors, and increasing the V$_{Ga}$ concentration which compensates the unintentional doping. At the same time, as can be seen in Fig. 4.6, it makes O$_i^0$ the dominant hole trap by far. This explains the green PL in this sample (with octahedral V$_{Ga}^{-1}$ and (V$_{Ga}$ + V$_O$)$^{1-}$ contributing some blue emission), without the involvement of an impurity. Comparing the middle and the right diagram in Fig. 4.6, I note that a shift towards Ga-rich conditions would increase the formation energy of V$_{Ga}$, (V$_{Ga}$ + V$_O$), and O$_i$ and decrease that of V$_O$. So I predict the decrease of the blue and green and increase of the IR-red PL in Ga-rich samples.
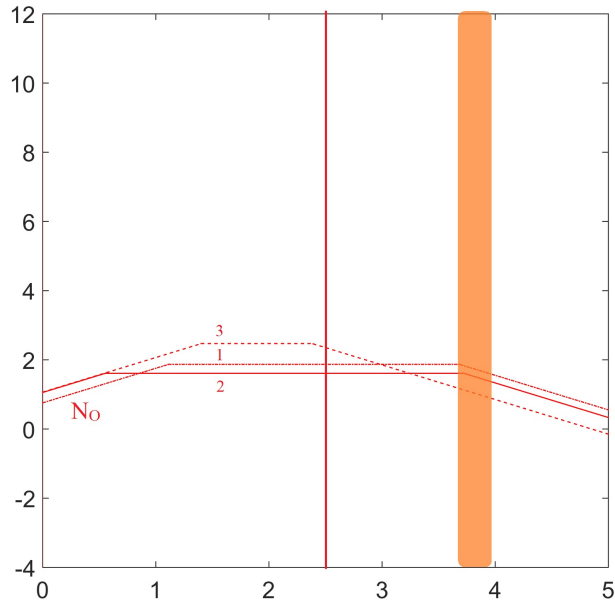

Figure 4.7: Formation energies (eV), as a function of the Fermi-level position. N$_O$ was calculated assuming a nitrogen-rich environment of a nearly stoichiometric sample.

The assignment of the N-related PL at 1.8 eV to the peak observed in bulk-like single crystals can be justified as follows. The growth conditions described in Ref.[15] make it likely that the as grown samples are nearly stoichiometric (or at most slightly oxygen-poor). The doping followed by heating in an NH_3 atmosphere. I consider the chemical potential of nitrogen in this environment to be limited by GaN formation (which obviously happens upon prolonged annealing [15]). The formation energy of N_O under such circumstances is shown in Fig. 4.7 Since the samples were not intentionally doped, [15] I may assume that the Fermi-level is near midgap, due to the compensating effect of the nitrogen acceptors incorporated in high concentration. In that region the neutral charge state of N_O is stable, and the three-fold coordinated sites are energitically preferred. The latter yield PL values of 1.78 eV and 1.79 eV, respectively.

4. Doping with Mg, hyperfine and deep acceptor behaviors

At present, it is very challenging to make β-Ga_2O_3 p-type. Based on its success in GaN, magnesium (Mg) has been suggested as a p-type dopant in β-Ga_2O_3 as well [60, 61]. However, It has lead to semi-insulating behavior because of deep acceptor levels of Mg at Ga site [55, 62, 63]. In a recent experimental study, Kananen and his colleagues [3] have confirmed the deep acceptor behavior of Mg in β-Ga_2O_3 by using electron paramagnetic resonant techniques (EPR). The EPR results were explained by a trapped hole on oxygen site, adjacent to the Mg acceptor

has the EPR interaction with Ga sites around.

Here, I study the behaviors of a Mg substitutional at the Ga sites (Mg_{Ga}), by using the optimized hybrid functional HSE(0.26,0.00). The calculated the formation energies of Mg_{Ga}, in the neutral and singly negative charge states are shown in Fig 4.8, as a function of the Fermi-level position between the two band edges. The applied chemical potentials correspond to O-rich, $\left(\mu_O = \frac{1}{2}\mu^{O_2}\right)$ and and Mg-rich $\left(\mu_{Mg} = \mu^{MgO} - \mu_O\right)$ conditions
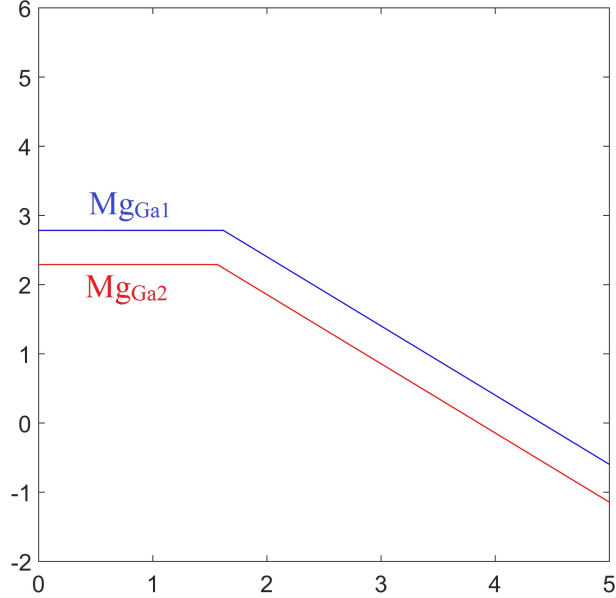
Figure 4.8: Formation energy (eV) of Mg_{Ga} under oxygen-rich conditions, as a function of the Fermi-level position.

Mg in β-Ga_2O_3 can substitute Ga at Ga1 or/and Ga2 site. The calculation has shown that Mg_{Ga2} is significantly more favorable than Mg_{Ga1} energitically, in agreement with an earlier study [33]. This could be due to the fact that the Mg^{2+} radius is larger than the Ga^{3+} radius, thus Mg prefers occupying a six-

coordinated Ga2 site because Ga2 has more space for a bigger impurity than four-coordinated Ga1 site. The charge transition levels show deep acceptor behavior. The (0/-1) level is calculated to be at 1.57 eV and 1.62 eV above the valence band edge for Mg_{Ga2} and Mg_{Ga1}, respectively. These levels are much too deep for Mg to be considered as an effective p-type dopant. They rather act as electron traps, compensating the unintentional n-type doping. This explains why Mg-doped β-Ga_2O_3 is semi-insulating. Because of the compensation between Mg acceptor and the Si donors, Mg is present as Mg^{1-}, with no unpaired spin, that explains why no EPR signal was measured by Kananen $et~al.$ [3] without X-ray irradiation. After the irradiation, a hole is trapped by Mg^{1-}. The hole localizes at nearly oxygen site, in a state which can be considered as a small polaron. It has been shown that holes can be self-trapped at O1 and O2 sites, but not at the O3 site. The calculated formation energies of the trapped holes near Mg (Fig. 4.9) show that the hole is more favorable at the O1 site (OTH1) than at O2 (OTH2), by 0.1 eV. This result is consistent with the suggestion of Kananen $et~al.$ [3]

The natural abundance of the ^{16}O isotope, with no nuclear spin, is more than 99% while that of ^{17}O with nuclear spin I = 5/2 is only $3.8.10^{-4}$ that is too small to detect the hyperfine interaction of the unpaired spin with oxygen. The gallium isotopes, with 60.1% and 39.9% abundance for ^{69}Ga and ^{71}Ga, respectively, have both I = 3/2, so a hyperfine interaction with the two Ga neighbours of O, where the hole is trapped, can be expected. Because the percentage of the ^{25}Mg nuclei is just 10%, and its nuclear gyromagnetic ratio is small (around 4 times smaller than ^{69}Ga), Mg related HFI is not expected to show up in the experiment.
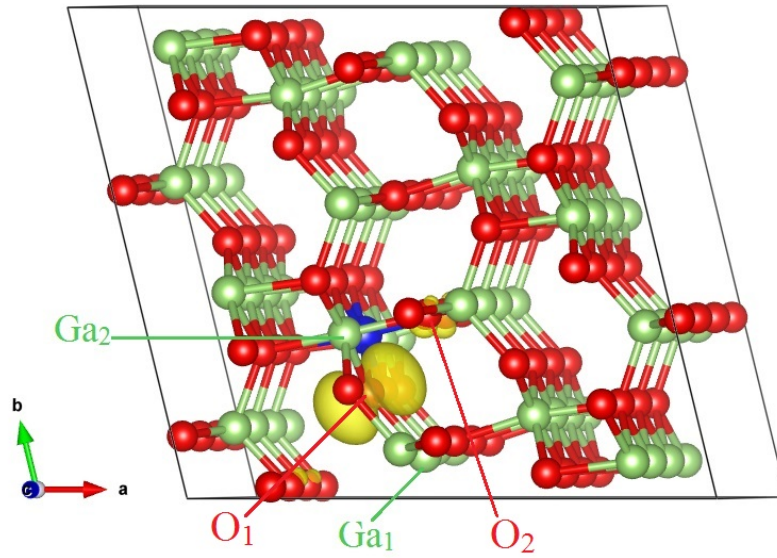
Figure 4.9: The yellow lobes show a trapped hole at an oxygen O1 site adjacent to Mg_{Ga2} (blue). The trapped hole has superhyperfine interaction with a Ga2 and a Ga1 atom.

Table 4.5: The superhyperfine interaction of the trapped-hole with Ga (^{69}Ga isotope) sites from HSE(0.26,0.0) calculation and from experiment.[3]

Site	HSE(0.26,0.0) (MHz)			Experiment (MHz) [3]		
	a	b	c	a	b	c
Ga1	76.32	81.17	72.14	73.15	71.74	71.46
Ga2	40.43	41.21	39.78	33.07	33.35	31.67
ratio	1.89	1.95	1.81	2.21	2.15	2.16

The hyperfine values calculated for ^{69}Ga are listed in Table 4.5 for the three crystallographic directions, together with the experimental values. The hyerfine interaction with Ga1 is a factor of 1.9 larger than with Ga2. This is the consequence of the fact that the distances from the O1 site (where the hole localizes) to Ga1 and Ga2 sites are 1.918 Å and 2.095 Å, respectively. In the calculation, the Fermi contact part of the hyperfine interaction on Ga sites is dominant, while the dipolar part is almost zero. This is in line with the isotropic nature found in the EPR measurement. [3]

Chapter 5

Conclusions

1. Work performed

In this thesis, I have studied the electronic structure and formation energies of intrinsic defects, the PL energy, and the hyperfine interaction of a hole trapped by Mg_{Ga} with Ga neighbours in β-Ga_2O_3. My calculations are based on the hybrid functional that the paramaters, $\alpha = 0.26$ and $\mu = 0.00$, are optimized for to reproduce the experimental band gap and fulfill the generalized Koopmans' theorem. In charge correction calculations, I used the high-frequency bulk dielectric constant ε_∞ for both of vertical and adiabatic charge transitions. I got the results as follows:

- Transition levels from my calculations agree very well to the experimental results, and from those results, I am able to give a consistent description of observed carrier trapping by intrinsic defects in β-Ga_2O_3.

- I assign the DLTS peaks at CBM - 0.75 eV, and -1.04 eV to V_{Ga1}(2-/3-) and V_{Ga2}(2-/3-), respectively. The DLOS peaks at CBM - 2.16 eV and - 4.40 eV are explained by V_O(2+/0) and h^+(+/0). The EELS peak at 3.3 eV is attributed to the average vertical transition of oxygen vacancies while a series of optical absorption peaks beginning at 4.48 eV are assigned to V_{Ga} and O_i.

- V_{Ga} is the main compensating intrinsic defect of n-type β-Ga_2O_3. Ga_i can contribute to the n-type conductivity of β-Ga_2O_3 at low temperature. V_O, O_i, and $V_{Ga}-V_O$ are hole trap centers. Self-trapping holes are found as small hole polarons at O1 and O2 sites (no small polaron at O3 site).

- PL in β-Ga_2O_3 is the result of the recombination between an electron in a shallow donor state and a trapped hole. The doping asymmetry of wide-band-gap semiconductors is well known: most of them can only be doped either n- or p- type [101], with only deep acceptors in the former and deep donors in the later. The PL mechanism in β-Ga_2O_3 is also suggested as a general mechanism in wide-band gap semiconductors that can only be doped with n-type dopants. The UV PL is assigned to the self-trapped holes, the blue PL is primarily due to $V_{Ga}-V_O$ (with a minor contribution from V_{Ga}), and the green originates mainly from O_i. My suggestions are supported by the observed polarization properties of the UV band and by the intensity variations of the blue and green bands depending on carrier concentration and stoichiometry. My calculated results of N_O yield a red PL that agrees very with the experimental measurement.

- Substitutional Mg in β-Ga_2O_3 was studied and the results showed that Mg_{Ga} is a deep acceptor with Mg_{Ga2} being more stable than Mg_{Ga1}. A hole trapped by O1 the nearest neighbour of Mg_{Ga2} has hyperfine interactions with 2 Ga neighbours. The hyperfine parameter at Ga1 site is around 1.9 times larger than at Ga2 site. My calculations agree very well to the experimental EPR spectra in a Mg-doped β-Ga_2O_3 sample.

2. Future work

In my thesis, I have shown that the calculated results from the optimized hybrid functional, which the parameters were chosen based on the criteria of fitting one-particle gap and fulfilling the generalized Koopmans' theorem. The optimized hybrid functional provides a consistent interpretation of a wide range of experimental observations and explains origin of photoluminescence in β-Ga_2O_3. Deák *et al.* [2] have suggested that the same procedure can also be applied for other materials. In my future work, I will choose the optimized hybrid functional for ZnS and then I will use that optimzed hybrid functional to study defects and explain origin of luminescence in extrinsic samples.

Bibliography

[1] J. Furthmüller and F. Bechstedt, Phys. Rev. B **93**, 115204 (2016).

[2] P. Deák, Q. D. Ho, F. Seemann, B. Aradi, M. Lorke, and T. Frauenheim, Physical Review B **95**, 075208 (2017).

[3] B. E. Kananen, L. E. Halliburton, E. M. Scherrer, K. T. Stevens, G. K. Foundos, K. B. Chang, and N. C. Giles, Appl. Phys. Lett. **111**, 072102 (2017).

[4] C. Wöll, Prog. Surf. Sci. **82**, 55 (2007).

[5] S. Nakamura, M. Senoh, and T. Mukai, Appl. Phys. Lett. **62**, 2390 (1993).

[6] H. Morkoç, S. Strite, G. B. Gao, M. E. Lin, B. Sverdlov, and M. Burns, J. Appl. Phys. **76**, 1363 (1994).

[7] Y. Tomm, P. Reiche, D. Klimm, and T. Fukuda, J. Cryst. Growth **220**, 510 (2000).

[8] H. Aida, K. Nishiguchi, H. Takeda, N. Aota, K. Sunakawa, and Y. Yaguchi, Jpn. J. Appl. Phys. **47**, 8506 (2008).

[9] O. Takayoshi, K. Kaminaga, H. Mashiko, A. Mukai, K. Sasaki, T. Masui, A. Kuramata, S. Yamakoshi, and A. Ohtomo, Jpn. J. Appl. Phys. **52**, 111102 (2013).

[10] H. Yoshida and K. Maeda, Stud. Surf. Sci. Catal. **175**, 351 (2010).

[11] Y. Hou, X. Wang, L. Wu, Z. Ding, and X. Fu, Environ. Sci. Technol. **40**, 5799 (2006).

[12] Y. Hou, L. Wu, X. Wang, Z. Ding, Z. Li, and X. Fu, J. Catal. **250**, 12 (2007).

[13] T. Minami, T. Shirai, T. Nakatani, and T. Miyata, Jpn. J. Appl. Phys. **39**, L524 (2000).

[14] T. Miyata, T. Nakatani, and T. Minami, J. Lumin. **87**, 1183 (2000).

[15] T. T. Zhang, J. Lin, X. Zhang, Y. Huang, X. Wu, Y. Xue, J. Zou, and C. Tang, J. Lumin. **140**, 30 (2013).

[16] K. Bernhardt, M. Fleischer, and H. Meixner, Siemens Compon. **30**, 35 (1995).

[17] M. Fleischer and H. Meixner, Sensors and Actuators B **5**, 115 (1991).

[18] M. Bartic, Phys. Stat. Sol. A **213**, 457 (2016).

[19] M. Fleischer, S. Kornely, T. Weh, J. Frank, and H. Meixner, Sens. and Act. B **69**, 205 (2000).

[20] J. Kohn, G. Katz, and J. D. Broder, Am. Mineral. **42**, 398 (1956).

[21] M. Saurat and A. Revcolevschi, Rev. Int. Hautes. Refract. **8**, 291 (1971).

[22] P. Kroll, R. Dronskowski, and M. Martin, J. Mater. Chem. **15**, 3296 (2005).

[23] H. He, M. A. Blanco, and R. Pandey, Appl. Phys. Lett. **88**, 261904 (2006).

[24] S. Yoshioka, H. Hayashi, A. Kuwabara, F. Oba, K. Matsunaga, and I. Tanaka, J. Phys.: Condens. Matter **19**, 346211 (2007).

[25] H. Y. Playford, A. C. Hannon, E. R. Barney, and R. I. Walton, Chem.-A Eur. J. **19**, 2803 (2013).

[26] S. I. Stepanov, V. I. Nikolaev, V. E. Bougrov, and A. E. Romanov, Rev. Adv. Mater. Sci. **44**, 63 (2016).

[27] H. V. Wenckstern, Adv. Electron. Mater. **3**, 1600350 (2017).

[28] H. H. Tippins, Phys. Rev. B **140**, A316 (1965).

[29] M. Orita, H. Ohta, M. Hirano, and H. Hosono, Appl. Phys. Lett. **77**, 4166 (2000).

[30] K. E. Lipinska-Kalita, P. E. Kalita, O. A. Hemmers, and T. Hartmann, Phys. Rev. B **77**, 094123 (2008).

[31] H. He, R. Orlando, M. A. Blanco, R. Pandey, E. Amzallag, I. Baraille, and M. Rérat, Phys. Rev. B **74**, 195123 (2006).

[32] J. B. Varley, J. R. Weber, A. Janotti, and C. G. V. d. Walle, Appl. Phys. Lett. **97**, 142106 (2010).

[33] C. Tang, J. Sun, N. Lin, Z. Jia, W. Mu, X. Tao, and X. Zhao, RSC Advances **6**, 78322 (2016).

[34] L. L. Liu, M. K. Li, and D. Q. Yu, J. Appl. Phys. A **98**, 831 (2010).

[35] L. Dong, R. Jia, C. Li, B. Xin, and Y. Zhang, J. Alloy. Compd. **712**, 379 (2017).

[36] N. Ueda, H. Hosono, R. Waseda, and H. Kawazoe, Appl. Phys. Lett. **70**, 3561 (1997).

[37] N. Suzuki, S. Ohira, M. Tanaka, T. Sugawara, K. Nakajima, and T. Shishido, Phys. Status Solidi C **4**, 2310 (2007).

[38] K. Sasaki, A. Kuramata, T. Masui, E. G. Vıllora, K. Shimamura, and S. Yamakoshi, Appl. Phys. Express **5**, 035502 (2012).

[39] E. G. Vıllora, K. Shimamura, Y. Yoshikawa, T. Ujiie, and K. Aoki, Appl.Phys. Lett. **92**, 202120 (2008).

[40] K. Sasaki, M. Higashiwaki, A. Kuramata, T. Masui, and S. Yamakoshi, J. Cryst. Growth **378**, 591 (2013).

[41] M. Marezio and J. P. Remeika, J. Chem. Phys. **46**, 1862 (1967).

[42] K. Irmscher, Z. Galazka, M. Pietsch, R. Uecker, and R. Fornari, J. Appl. Phys. **110**, 063720 (2011).

[43] Z. Hajnal, J. Miró, G. Kiss, F. Réti, P. Deák, R. C. Herndon, and J. M. Kuperberg, J. Appl. Phys. **86**, 3792 (1999).

[44] M. Yamaga, H. Tsuzuki, S. Takano, E. G. Villora, and K. Shimamura, J. Non-Cryst. Solids **358**, 2458 (2012).

[45] N. T. Son, K. Goto, K. Nomura, Q. T. Thieu, R. Togashi, H. Murakami, Y. Kumagai, A. Kuramata, M. Higashiwaki, A. Koukitu, S. Yamakoshi, B. Monemar, and E. Janzén, J. Appl. Phys. **120**, 235703 (2016).

[46] A. Kuramata, K. Koshi, S. Watanabe, Y. Yamaoka, T. Masui, and S. Yamakoshi, Jpn. J. Appl. Phys. **55**, 1202A2 (2016).

[47] G. Schmitz, P. Gassmann, and R. Franchy, J. Appl. Phys. **83**, 2533 (1998).

[48] L. Binet and D. Gourier, Appl. Phys. Lett. **77**, 1138 (2000).

[49] Z. Zhang, E. Farzana, A. R. Arehart, and S. A. Ringel, Appl. Phys. Lett. **108**, 052105 (2016).

[50] A. I. Kuznetsov, V. N. Abramov, and T. V. Uibo, Opt. Spectrosc. (USSR) **58**, 368 (1985).

[51] M. Yamaga, T. Ishikawa, M. Yoshida, T. Hasegawa, E. G. Víllora, and K. Shimura, Phys. Stat. Sol. C **8**, 2621 (2011).

[52] M. Michling and D. Schmeißer, IOP Conf. Ser.: Mater. Sci. Eng. **34**, 012002 (2012).

[53] L. Binet and D. Gourier, J. Phys. Chem. Solids **59**, 1241 (1998).

[54] T. Harwig and F. J. Kellendonk, Solid State Chem. **24**, 255 (1978).

[55] T. Onuma, S. Fujioka, T. Yamaguchi, M. Higashiwaki, K. Sasaki, T. Masui, and T. Honda, Appl. Phys. Lett. **103**, 041910 (2013).

[56] E. G. Víllora, M. Yamaga, T. Inoue, S. Yabasi, Y. Masui, T. Sugawara, and T. Fukuda, Jpn. J. Appl. Phys. **41**, L622 (2002).

[57] G. Pozina, M. Forsberg, M. A. Kaliteevski, and C. Hemmingson, Sci. Rep. **7**, 42132 (2017).

[58] Y. P. Song, H. Z. Zhang, C. Lin, Y. W. Zhu, G. H. Li, F. H. Yang, and D. P. Yu, Phys. Rev. B **69**, 075304 (2004).

[59] L. W. Chang, T. Y. Lu, Y. L. Chen, J. W. Yeh, and H. C. Shih, Mater. Lett. **65**, 2281 (2011).

[60] S. Nakamura, T. Mukai, M. Senoh, and N. Iwasa, Jpn. J. Appl. Phys., Part 2 **31**, L139 (1992).

[61] P. Pampilia and P. J. Parbook, Mater. Sci. Semicond. Process **62**, 180 (2017).

[62] Z. Galazka, K. Irmscher, R. Uecker, R. Bertram, M. Pietsch, A. Kwasniewski, M. Naumann, T. Schulz, R. Schewski, D. Klimm, and M. Bickermann, J. Cryst. Growth **404**, 184 (2014).

[63] X. Feng, Z. Li, W. Mi, and V. J. Ma, Vacuum **124**, 101 (2016).

[64] P. Hohenberg and W. K. 136, Phys. Rev. **136**, B864 (1964).

[65] W. Kohn and L. Sham., Phys. Rev. **140**, A1133 (1965).

[66] R. G. Parr and W. Yang., Oxford University Press (1994).

[67] W. R. L. Lambrecht, Phys. Stat. Sol. (b) **248**, 1547 (2011).

[68] C. Freysoldt, B. Grabowski, T. Hickel, J. Neugebauer, G. Kresse, A. Janotti, and C. G. V. d. Walle, Rev. Mod. Phys. **86**, 253 (2014).

[69] G. Sai and L. Bang-Gui, Chin. Phys. B **21**, 057104 (2012).

[70] H. Tang, K. Prasad, R. Sanjinès, P. E. Schmid, and F. Lévy, J. Appl. Phys. **75**, 2042 (1994).

[71] S. J. Clark and J. Robertson, Phys. Rev. B **82**, 085208 (2010).

[72] X. Zheng, A. J. Cohen, P. Mori-Sanchez, X. Hu, and W. Yang, Phys. Rev. Lett. **107**, 026403 (2011).

[73] J. Heyd, G. E. Scuseria, and M. Ernzerhof, J. Chem. Phys. **118**, 8207 (2003).

[74] A. V. Krukau, O. A. Vydrov, A. F. Izmaylov, and G. E. Scuseria, J. Chem. Phys. **125**, 224106 (2006).

[75] J. P. Perdew, M. Ernzerhof, and K. Burke, J. Chem. Phys. **105**, 9982 (1996).

[76] C. Adamo and V. Barone, J. Chem. Phys. **110**, 6158 (1999).

[77] J. Paier, M. Marsman, K. Hummer, G. Kresse, I. C. Gerber, and J. G. Ángyán, J. Chem. Phys. **124**, 154709 (2006).

[78] M. Marsman, J. Paier, A. Stroppa, and G. Kresse, J. Phys.: Condens. Matter **20**, 064201 (2008).

[79] F. Fuchs, J. Furthmüller, F. Bechstedt, M. Siskin, and G. Kresse, Phys. Rev. B **76**, 115109 (2007).

[80] S. Lany and A. Zunger, Phys. Rev. B **80**, 085202 (2009).

[81] G. Kresse and J. Hafner, Phys. Rev. B **49**, 14251 (1994).

[82] G. Kresse and J. Furthmüller, ibid **54**, 11169 (1996).

[83] G. Kresse and D. Joubert, ibid **59**, 1758 (1999).

[84] H. J. Monkhorst and J. K. Pack, Phys. Rev. B **13**, 5188 (1976).

[85] F. D. Murnaghan, Proc. Natl. Acad. Sci. USA **30**, 244 (1944).

[86] P. Deák, B. Aradi, and T. Frauenheim, Phys. Rev. B **86**, 195206 (2012).

[87] C. Freysoldt, J. Neugebauer, and C. G. V. d. Walle, Phys. Rev. Lett. **102**, 016402 (2009).

[88] W. Chen and A. Pasquarello, Phys. Rev. B **88**, 115104 (2013).

[89] S. Lany and A. Zunger, Phys. Rev. B **78**, 235104 (2008).

[90] M. Mohamed, C. Janowitz, I. Unger, R. Manzke, Z. Galazka, R. Uecker, R. Fornari, J. R. Weber, J. B. Varley, and C. G. V. d. Walle, Appl. Phys. Lett. **97**, 211903 (2010).

[91] H. Peelaers and C. G. V. d. Walle, Phys. Status Solidi B **252**, 828 (2015).

[92] J. Åhman, G. Svensson, and J. Albertsson, Acta Crystallogr., Sect. C: Cryst. Struct. Commun. **52**, 1336 (1996).

[93] T. Zacherle, P. C. Schmidt, and M. Martin, Phys. Rev. B **87**, 235206 (2013).

[94] A. M. d. Santos, D. Beliaev, L. M. R. Scolfaro, and J. R. Leite, Brazilian J. Phys. **29**, 775 (1999).

[95] S. Hava and M. Auslender, J. Quant. Spectrosc. Radiat. Transfer **49**, 259 (1993).

[96] J. B. Varley, H. Peelaers, A. Janotti, and C. G. V. d. Walle, J. Phys.: Cond. Matter. **23**, 334212 (2011).

[97] J. B. Varley, A. Janotti, C. Franchini, and C. G. V. d. Walle, Phys. Rev. B **85**, 081109(R) (2012).

[98] P. B. A. Alkauskas and A. Pasquarello, Phys. Rev. Lett. **101**, 046405 (2008).

[99] M. E. Ingebrigtsen, J. B. Varley, A. Y. Kuznetsov, B. G. Svensson, G. Alfieri, A. Mihaila, U. Badstübner, and L. Vines, Appl. Phys. Lett. **112**, 042104 (2018).

[100] A. Kyrtsos, M. Matsubara, and E. Belotti, Appl. Phys. Lett. **112**, 032108 (2018).

[101] H. Yan and S. H. Wei, Phys. Stat. Sol. (b) **245**, 641 (2008).